An experimental study into the flow physics of three-dimensional shock control bumps

P.J.K. Bruce[1] and H. Babinsky[2]
Department of Engineering, University of Cambridge,

Trumpington Street, Cambridge, CB2 1PZ, UK

This paper describes a fundamental experimental study of the flow structure around a single three-dimensional (3-D) transonic shock control bump (SCB) mounted on a flat surface in a wind tunnel. Tests have been carried out with a Mach 1.3 normal shock wave located at a number of stream-wise positions relative to the SCB. A range of experimental techniques have been used to study details of the flow. The results of the work build on the findings of previous researchers and shed new light on the flow physics of 3-D SCBs. It is found that span-wise pressure gradients across the SCB ramp affect the magnitude and uniformity of flow-turning generated by the bump, which can impact on the span-wise propagation of the quasi-2-D shock structure produced by a 3-D SCB. At the bump crest, vortices can form if the pressure on the crest is significantly lower than at either side of the bump. The trajectories of these vortices, which are relatively weak, are strongly influenced by any span-wise pressure gradients across the bump tail. A significant difference between 2-D and 3-D SCBs highlighted by the study is the impact of span-wise pressure gradients on 3-D SCB performance. The magnitude of these span-wise pressure gradients is determined largely by SCB geometry and shock position.

---

[1] Research Associate, Member AIAA
[2] Professor in Aerodynamics, AIAA Associate Fellow

Nomenclature

C_f	= Skin friction coefficient
$H \equiv \frac{\delta^*}{\theta}$	= Compressible boundary layer shape factor
$H_i \equiv \frac{\delta_i^*}{\theta_i}$	= Incompressible boundary layer shape factor
M_∞	= Freestream Mach number
$Re_{\delta^*} \equiv \frac{\rho U_\infty \delta^*}{\mu}$	= Reynolds number based on boundary layer displacement thickness
x, y, z	= Stream-wise, tunnel floor-normal, tunnel span-wise coordinates [mm]
x_s	= Stream-wise shock position relative to the bump tip [mm]
δ	= Boundary layer thickness (measured to 99% freestream velocity) [mm]
$\delta^* \equiv \int_0^\delta (1 - \frac{\rho u}{\rho_e u_e}) dy$	= Compressible boundary layer displacement thickness [mm]
$\delta_i^* \equiv \int_0^\delta (1 - \frac{u}{u_e}) dy$	= Incompressible boundary layer displacement thickness [mm]
$\theta \equiv \int_0^\delta \frac{\rho u}{\rho_e u_e}(1 - \frac{u}{u_e}) dy$	= Compressible boundary layer momentum thickness [mm]
$\theta_i \equiv \int_0^\delta \frac{u}{u_e}(1 - \frac{u}{u_e}) dy$	= Incompressible boundary layer momentum thickness [mm]

I. Introduction

Normal or near-normal shock waves occur on the wings of modern transonic aircraft and in supersonic engine intakes. Air which passes through these shock waves incurs a loss of stagnation pressure, which is a source of drag, known as *wave drag*, for transonic wings. This detrimental loss can be minimised by designing wings and intakes that operate with low shock strengths. However, the requirement of weak shock waves can limit the flight Mach number (M) of transonic aircraft and impose structural constraints on transonic wing design (e.g. wings must be very thin to reduce shock strength at high M). Engine intakes with weak shock waves require long subsonic diffusing sections downstream of the shock wave in order to slow the incoming flow down to sufficiently low velocities for entry to the compressor, which is undesirable for size and weight reasons. An alternative approach to reducing shock strength is to mitigate the high stagnation pressure losses incurred by strong shock waves through the application of shock control.

Shock control involves modifying (smearing) the shock structure close to the wing or engine intake surface in order to decelerate the flow more gradually (and hence more isentropically). Re-

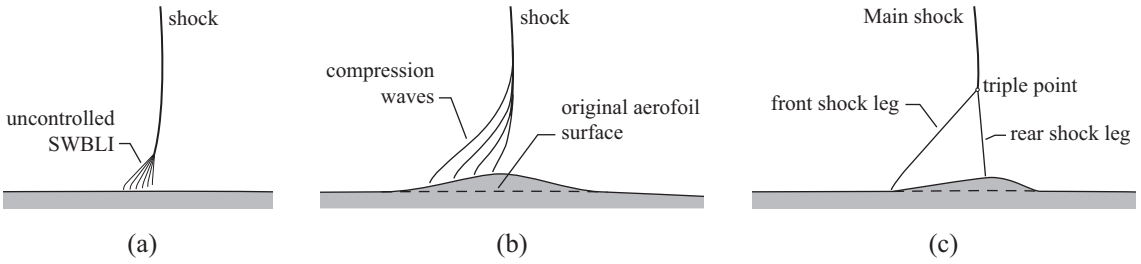

Fig. 1 Effect of SCBs on shock structure: (a) No-control case; (b) compression waves produced by a smooth contoured bump[3]; (c) λ-shock foot structure produced by a wedge bump[4]

search into both passive[1] and active[2] methods of shock control has been reported in the literature, although generally with rather limited success. However, one passive method of shock control which has shown promise is that of so-called shock control bumps (SCBs). These devices modify the local surface geometry in the region of a shock wave in order to split the shock into a number of weaker (oblique) shocks or compression waves close to the surface. SCBs typically consist of a ramp upstream of the nominal shock location (to generate an oblique shock ahead of the main shock wave and deflect the incoming supersonic flow away from the surface) followed by a tail (to bring the post-shock flow back to the surface). Figure 1 illustrates the shock structure produced by two different geometry SCBs.

Investigations have been performed with so-called two-dimensional (2-D) SCBs (where the bump shape is constant in the span-wise direction) by Ashill *et al.*[5]. They found that the use of a SCB significantly reduced overall drag when the shock wave was at its design location but incurred large performance penalties when the stream-wise shock position was varied. They attributed this poor robustness of SCB performance to variations in shock position to the appearance of undesirable expansions and secondary shock systems[4]. This sensitivity of SCB performance to shock position is a feature of this type of two-dimensional (2-D) SCB and is something that has been confirmed by other researchers[6, 7]. Figure 2, adapted from Ogawa *et al.*[4] shows the type of undesirable expansions and secondary shock systems that can be detrimental to SCB performance.

Recently, a number of studies have suggested that SCB robustness to variations in shock position can be improved by using an array of finite width - or three-dimensional (3-D) - SCBs instead of

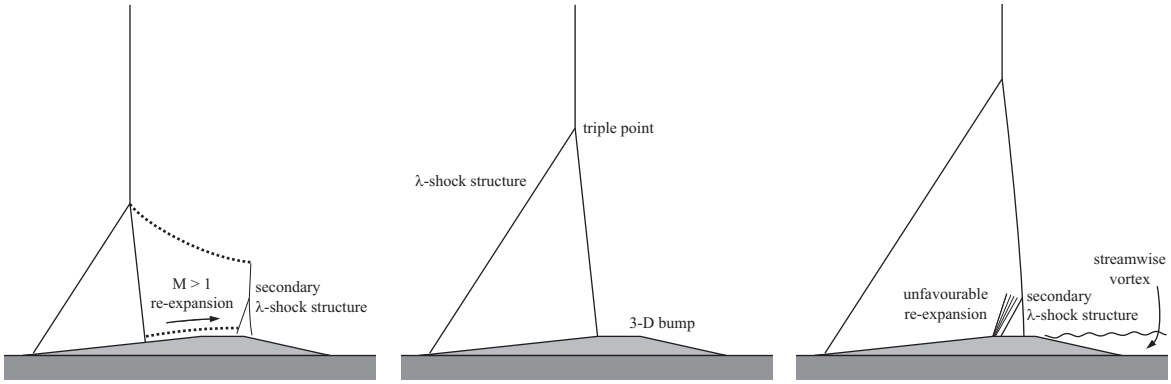

Fig. 2 Effect of shock position on SCB flow structure observed by Ogawa *et al.*[4]: (a) Shock upstream of optimum location; (b) at optimum location; (c) downstream of optimum location

a single 2-D device[4, 7–10]. Several of these studies have reported that 3-D SCBs are capable of delivering similar or even increased levels of performance benefit (drag saving) compared to 2-D devices with considerably improved robustness to shock position[7, 9]. Ogawa *et al.*[4] explain that the beneficial λ-shock structure produced by a 3-D SCB is quite two-dimensional and only decays gradually in span (see figure 3). As such, a span-wise array of carefully spaced discrete 3-D SCBs (spaced so that the shock structures produced by adjacent SCBs overlap) can produce a quasi-2-D beneficial shock structure across the entire span. König *et al.*[8] report that although smoothly contoured SCBs (figure 1b) give optimal drag reduction for the shock at its design point, wedge shaped devices (figure 1c) give improved robustness to variations in shock position with very little loss of efficiency.

A significant challenge in SCB design is to achieve beneficial stagnation pressure savings without incurring excessive viscous losses. In general, the flow curvature introduced by a SCB will be detrimental to the health of any incoming boundary layer. At the rear of a SCB in particular, flow separation can occur as the boundary layer is required to turn back towards the surface shortly after passing through a normal shock. In this respect, discrete 3-D SCBs may perform better than 2-D ones by localising any negative impact on the boundary layer to the regions directly behind the bumps. 3-D SCBs have also been observed to introduce stream-wise vorticity into the flow[4, 8, 10], which may be beneficial for delaying trailing edge separation on a wing[4, 10]. Ogawa *et al.* suggest

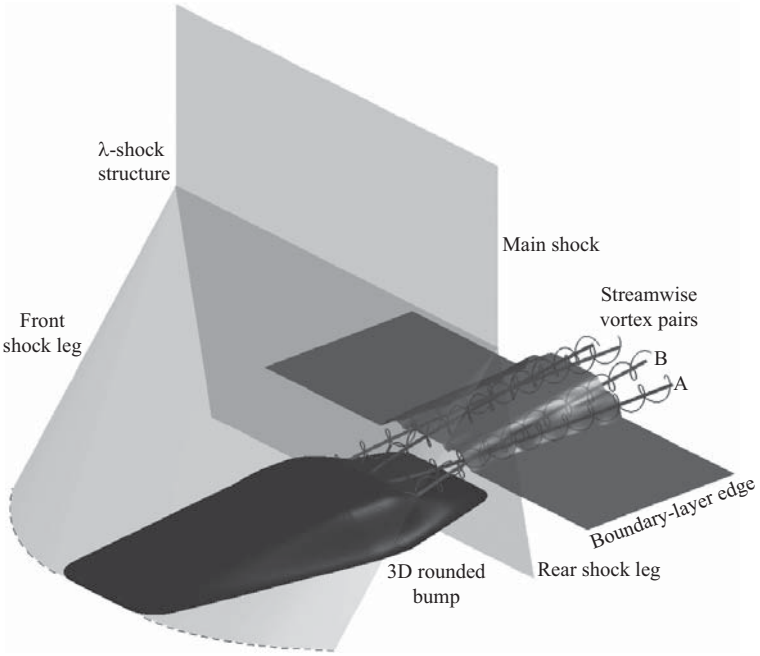

Fig. 3 Flow structure produced by a 3-D SCB, from Ogawa *et al.*[4]

that the vortical flow structures shown in figure 3 are caused by a combination of a strong adverse pressure gradient over the bump crest and a span-wise gradient over the bump sides.

Although previous research has provided some insight into the flow structure around 3-D bumps, it has often focused on quantifying the (positive or otherwise) global impact of factors such as bump height, ramp angle and shock strength on performance instead of developing our understanding of the detailed flow features. For this reason, our current knowledge of the complex interactions that occur in the presence of shock control is relatively immature and more fundamental research in this area is desirable. However, fundamental studies on complete configurations, such as an array of bumps on a wing, can be prohibitively expensive and a more economical approach is required. Computational studies offer an attractive alternative, although these currently struggle to capture some of the fine scale flow features on 3-D bumps due to resolution deficiencies, see for example[7].

The aim of this paper is to explore 3-D SCB flow physics through a series of fundamental wind tunnel experiments performed on an isolated simple-geometry SCB mounted on a flat surface at realistic flight conditions (in terms of shock strength and Reynolds number based on incoming boundary layer displacement thickness). Tests with a range of experimental techniques have been

performed to study the impact of variations in shock position and shock strength on features of the flow. Where relevant, the results are compared with the uncontrolled (no-bump) shock wave / boundary layer interaction that occurs in the wind tunnel. This analysis is used to address questions about bump flow physics (such as how two-dimensional the compression over the bump ramp is and how the quasi-2-D shock structure varies in the span-wise direction) and also to provide some insight into both aspects of SCB geometry that are critical to performance and how key flow features may be studied to allow a rapid and accurate assessment of SCB performance.

II. Experimental Methodology

Experiments have been performed in supersonic wind tunnel No. 1 at the Department of Engineering, University of Cambridge. The wind tunnel has a rectangular working section with a constant cross section 114 mm wide by 178 mm high. The experimental configuration used for the present study is shown in figure 4. Tests were performed with a uniform incoming Mach numbers of 1.3 (set by adjusting the tunnel throat geometry) in the parallel-walled working section. A movable shock-holding plate was used to enable accurate and stable positioning of the normal shock wave relative to the bump. This arrangement was developed and utilised for previous SCB studies in Cambridge[11]. Properties of the naturally grown incoming tunnel floor boundary layer with this configuration (measured on the tunnel centreline with no bump in the tunnel) are presented in table 1.

Table 1 Characteristic parameters of the incoming boundary layer in experiments. Incompressible values are given with compressible values in parentheses

P_0 (kPa)	M_∞	δ_0 (mm)	δ_0^* (mm)	θ_0 (mm)	H_{i0}	$Re_{\delta_0^*}$	C_f
180	1.3	4.6	0.62 (0.84)	0.45 (0.41)	1.36 (2.02)	(25,200)	0.00225

The SCB shape used has a simple geometry similar to the *default rounded* bump geometry defined and tested by Ogawa *et al.*[4], who reported it to be one of the most promising designs (in terms of total pressure saving) that they tested. In the present study, the height of the bump is approximately equal to the incoming boundary layer thickness δ_0. The bump, which is manufactured from plastic using rapid-prototyping techniques, has a total length equal to $30\delta_0$, made up of a $9\delta_0$

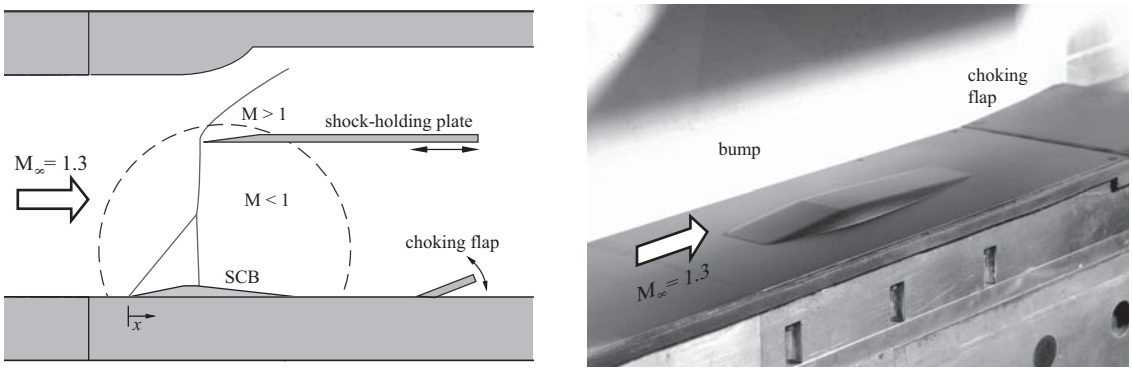

Fig. 4 Experimental arrangement: (a) Schematic diagram of the working section; (b) photograph. The area of optical access is shown as a dashed circle. The reference location $x = 0$ is defined as the start of the SCB ramp

long ramp followed by a gently rounded crest and a tail $18\delta_0$ long. The width of the bump varies continuously along its length, with a maximum width of $10\delta_0$ around the crest location.

The shock position relative to the SCB x_s is defined as the streamwise distance from the upstream tip of the bump to the shock and was set by moving the shock holding plate and adjusting the position of the choking flap. The wind tunnel is a blow-down facility and run times of up to 40 seconds were possible with the configuration shown in figure 4. Experimental techniques of schlieren photography, surface oil-flow visualisation, Pressure Sensitive Paint (PSP) and Laser Doppler Anemometry (LDA) have been used to interrogate the flow.

The pressure sensitive paint system was calibrated in situ using calibrated DRUCK PDCR-200 series pressure transducers to measure the pressure at eight locations on the bump surface and wind tunnel floor. Due to the sensitivity of the paint to variations in surface thermal properties, separate calibrations were neccessary for the (plastic) bump surface and (steel) tunnel floor. As a result of this sensitivity, the main source of experimental error in pressure measurements from PSP is due to regions where the surface thermal properties are not constant (such as towards the trailing edge of the SCB where the plastic is very thin). The maximum errors associated with properties and features of the flow measured using the above experimental techniques are summarised in table 2.

Table 2 Determination of flow properties and estimated measurement errors

Property	Units	Method	Error	Error source
Shock position	mm	Schlieren	$\pm 0.2\delta_0$	image resolution, tunnel set-up
Shock angles	deg [°]	Schlieren	$\pm 0.5^\circ$	image resolution, best guess
Separation location(s)	mm	Oil-flow, LDA	$\pm 0.5\delta_0$	LDA resolution, oil flow methodology
Surface pressures	Pa	PSP	$\pm 5\%$	PSP paint sensitivity, surface temperature
Velocity	ms^{-1}	LDA	$\pm 0.5\%$	LDA calibration
Flow angle	deg [°]	LDA	$\pm 2\%$	LDA calibration
B-L parameters δ, δ^*, θ	mm	LDA	$\pm 5\%$	LDA calibration, integration

III. Results and Discussion

Results that characterise the uncontrolled SBLI are presented first, followed by a qualitative study of how the addition of a SCB affects the flow field for a range of shock positions. The flow over the SCB ramp is also studied and two test cases are then analysed in detail: Firstly, with the shock upstream of the SCB crest and then with the shock downstream of the SCB crest.

A. Uncontrolled $M_\infty = 1.3$ SBLI

The baseline flow in the clean wind tunnel at $M_\infty = 1.3$ is characterised in figure 5. The schlieren image (a) shows a weak compression fan ahead of the main shock, which is indicative of a weak interaction without separation. The surface oil-flow (b) and LDA velocity measurements (d) confirm that the boundary layer remains attached through the interaction. The PSP image and pressure profiles (c) show that the flow is reasonably two-dimensional, although there is a small variation in the pressure profile across the tunnel span. This difference is attributed to span-wise curvature of the shock wave and a slight over-expansion of the flow ahead of the shock in the centre of the tunnel (which causes the Mach number there to be slightly above $M_\infty = 1.3$).

B. Effect of shock position on SCB flow at $M_\infty = 1.3$

Schlieren images from tests at $M_\infty = 1.3$ with six different shock positions are presented in figure 6. All of the images show how the bump causes large-scale bifurcation of the normal shock

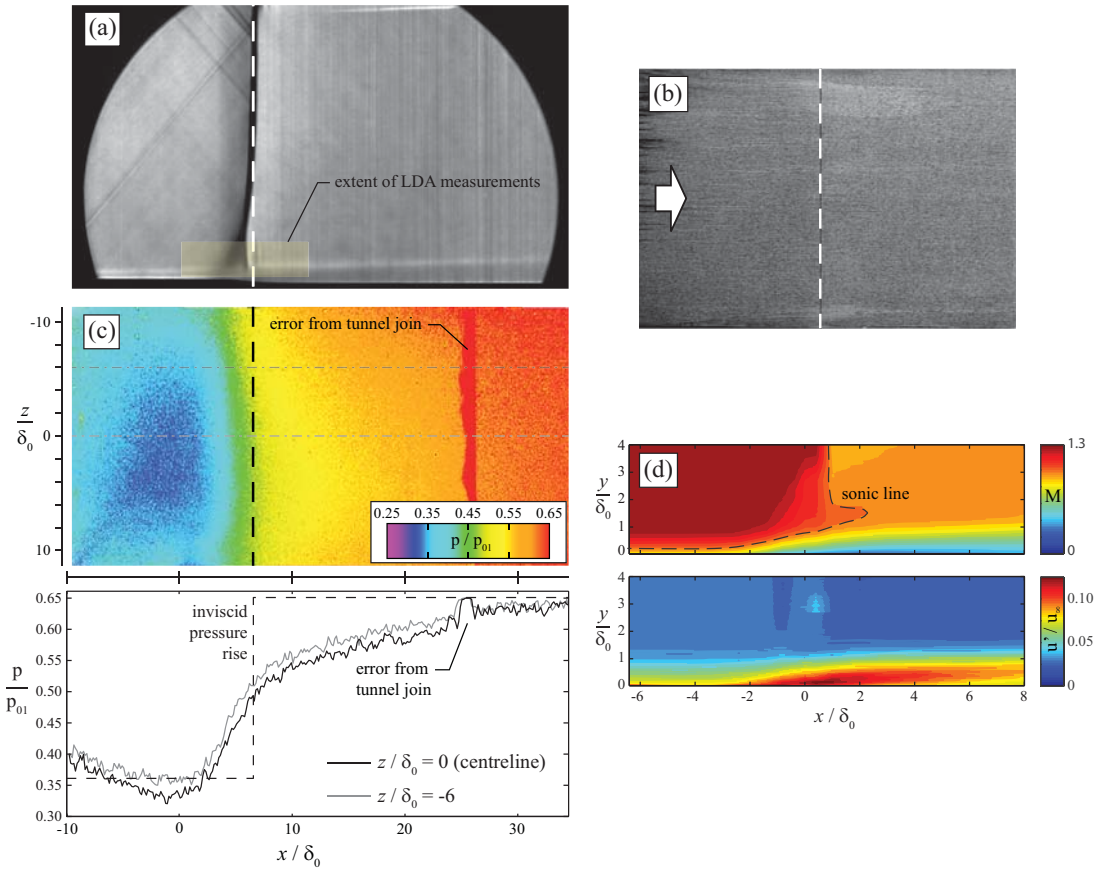

Fig. 5 Uncontrolled $M_\infty = 1.3$ shock wave / boundary layer interaction: (a) Schlieren photograph; (b) surface oil-flow visualisation; (c) surface pressure distribution from PSP and stream-wise pressure profiles at two span-wise stations; (d) stream-wise Mach number and velocity contours from LDA. The shock position for these tests is

wave, as observed by previous researchers (figure 1c). The size of the beneficial shock bifurcation region increases as the shock moves downstream. Variations in shock position upstream of the bump crest ($5 < x_s/\delta_0 < 11$) produce fairly benign changes in flow structure. When the shock is downstream of the bump crest ($x_s/\delta_0 = 13$ and 14), the (supersonic) flow over the bump crest is re-accelerated due to the convex bump curvature. This re-acceleration, which can be seen as an expansion fan in the schlieren images in figures 6(e)–(f), causes a local increase in the strength and curvature of the rear leg of the main λ-shock foot close to the bump. A secondary (local) lambda shock-foot structure can also be seen to appear in this region, which suggests that separation (or at least very rapid thickening) of the boundary layer is occurring. This is supported by the appearance

of a well-defined shear layer immediately downstream of the shock wave at $x_s/\delta_0 = 14$.

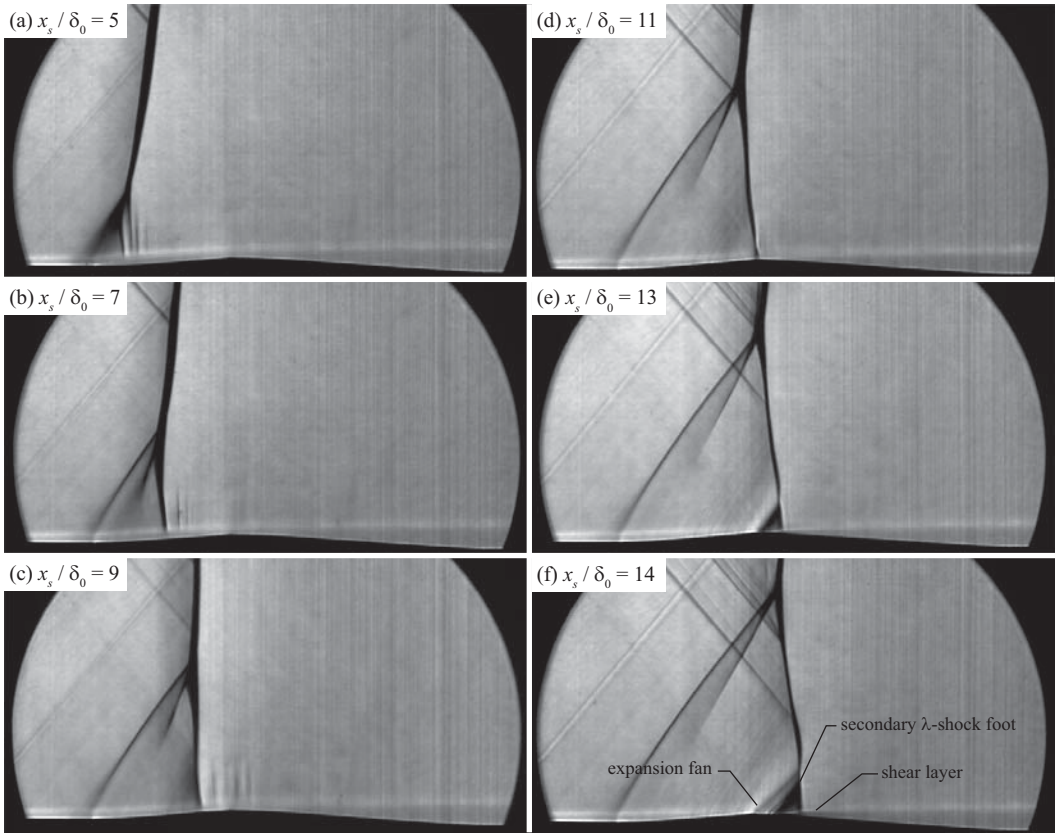

Fig. 6 Effect of shock position on SCB flow structure at $M_\infty = 1.3$

Surface oil-flow visualisations corresponding to the test cases in figure 6 are presented in figure 7. All of the images show evidence of strong span-wise variations of local shear stress downstream of the bump crest, indicated by dark and light patches of oil in the bump wake. This surface flow topography is typical of a flow which contains streamwise vortices, as illustrated in more detail for the $x_s/\delta_0 = 14$ test case in figure 8a. The oil-flow images in figure 7 suggest that shock positions downstream of the bump crest produce relatively large bump wakes, while shock positions upstream of the bump crest produce generally smaller wakes. However, the regions of high shear stress in the bump wake with $x_s/\delta_0 = 5$ do appear to be more strongly defined than they are when the shock is close to the bump crest ($x_s/\delta_0 = 9$). The region of oil accumulation just downstream of the bump crest when $x_s/\delta_0 = 14$ corresponds to a small separation bubble, which is shown in more detail in figure 8b. The lack of clearly-defined reversed flow in the separation region is caused by smearing of the oil during tunnel shut down.

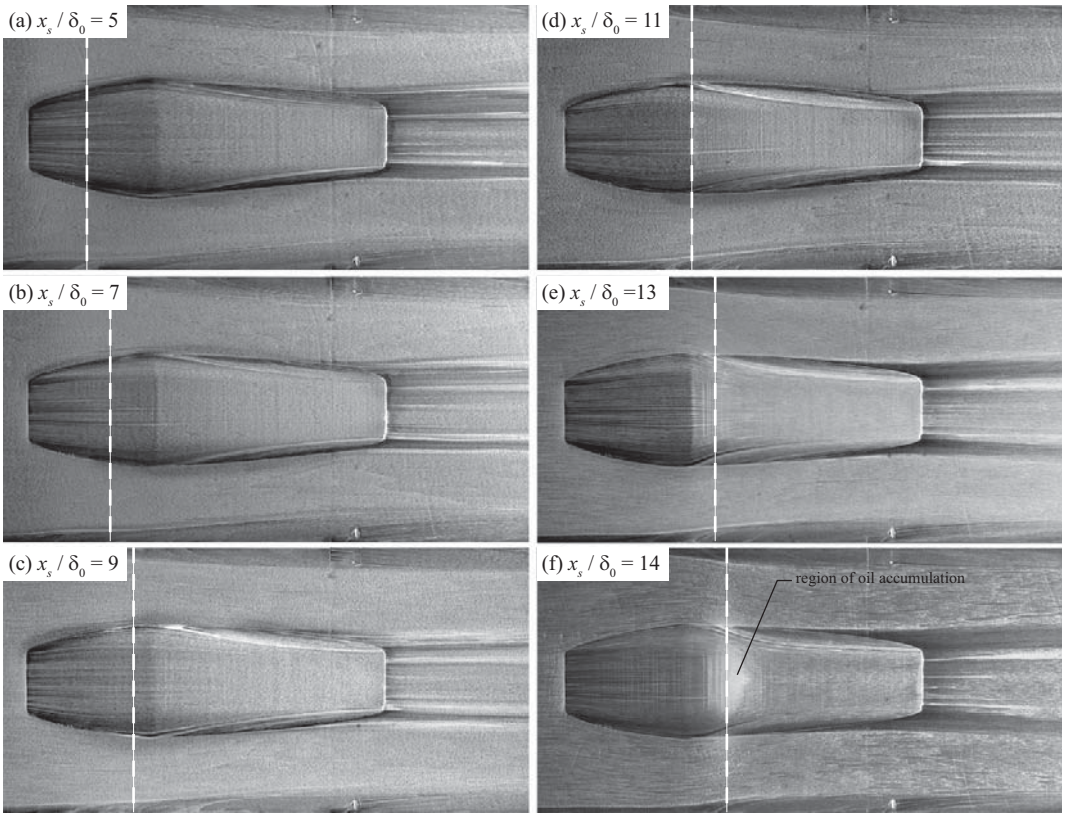

Fig. 7 Effect of shock position on surface flow topology at $M_\infty = 1.3$

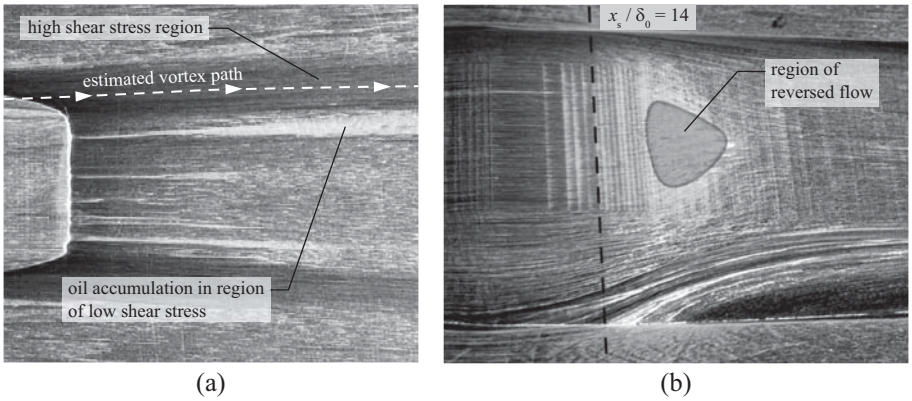

Fig. 8 Close up of SCB surface flow topology with $x_s/\delta_0 = 14$: (a) Vortices in the SCB wake; (b) separation bubble at the SCB crest

C. SCB ramp flow structure

The bifurcated shock structure produced by the SCB ramp with $x_s/\delta_0 = 9$ is studied in detail in figure 9. It can be seen that the front leg of the bifurcated shock system is not straight, which

suggests that the flow turning over the bump varies with vertical distance away from the wall (as the incoming Mach number is uniform throughout the tunnel). Close to the wall, the shock angle is approximately 60°, which corresponds to a flow turning angle of 4.7° (according to 2-D oblique shock theory). This is close to the bump ramp angle and suggests that the flow is relatively uniform close to the ramp. Further from the wall, the shock angle gradually decreases and tends to approximately 52.5°, which equates to a flow turning angle of just 1.5° (again, according to 2-D theory). This decrease in turning angle is expected as the effective flow turning angle for a three-dimensional bump is significantly smaller than the physical ramp angle. This is due to expansion effects from the sides of the bumps, which relieve part of the initial compression away from the bump surface by gradually reducing the flow turning angle. It is interesting to note that this shock angle of 52.5° is very close to the relevant conical shock angle for the bump geometry, which suggests that 3-D SCBs can be modelled as conical disturbances once a sufficient distance from the device is reached. As stated in table 2, the shock angles quoted above should be considered accurate only to within ±0.5°.

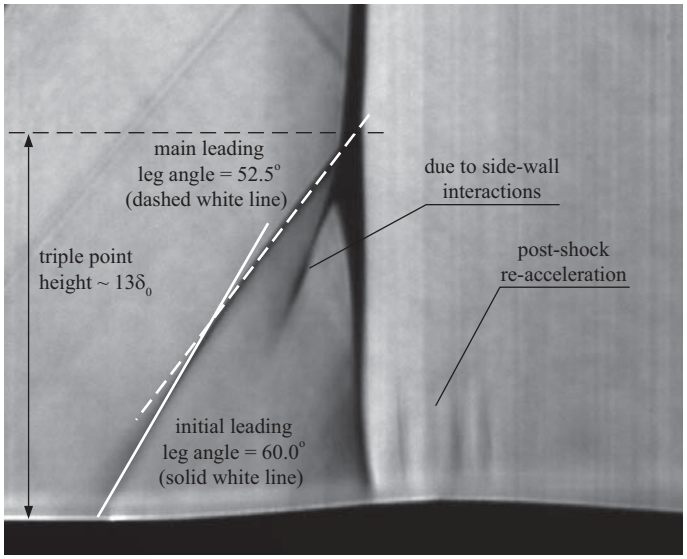

Fig. 9 Flow structure over the SCB ramp with $x_s/\delta_0 = 9$

Figure 9 also shows that re-acceleration of the post-shock flow to supersonic velocities occurs close to the SCB surface over the bump crest, immediately downstream of the rear leg of the λ-shock foot. This causes a series of weak "shocklets" to form behind the main shock, which are not thought

to have a significant effect on the flow. The dark line between the leading and main shock legs is thought to be caused by the interaction of the (curved) leading shock with the side-wall boundary layer and gives some indication of the extent of shock-front curvature.

Information on the wall-normal and span-wise variation of the flow turning angle over the bump ramp with $x_s/\delta_0 = 9$ is presented in figure 10. The flow angle contour plot in figure 10a shows that the flow deflection angle is highest close to the SCB surface and gradually decreases with distance away from the SCB, in agreement with previous observations. From this, it may be reasonable to assume that the bump behaves in a broadly similar fashion to a cone. However, figure 10b shows that the flow angle is relatively uniform in the span-wise direction away from the wall ($1.5 \leq y/\delta_0 \leq 4$) at around 60–80% of the ramp angle. This would not be the case for a cone, and suggests instead that the discrete bump produces a relatively 2-D shock structure that extends beyond the bump width in the span-wise direction.

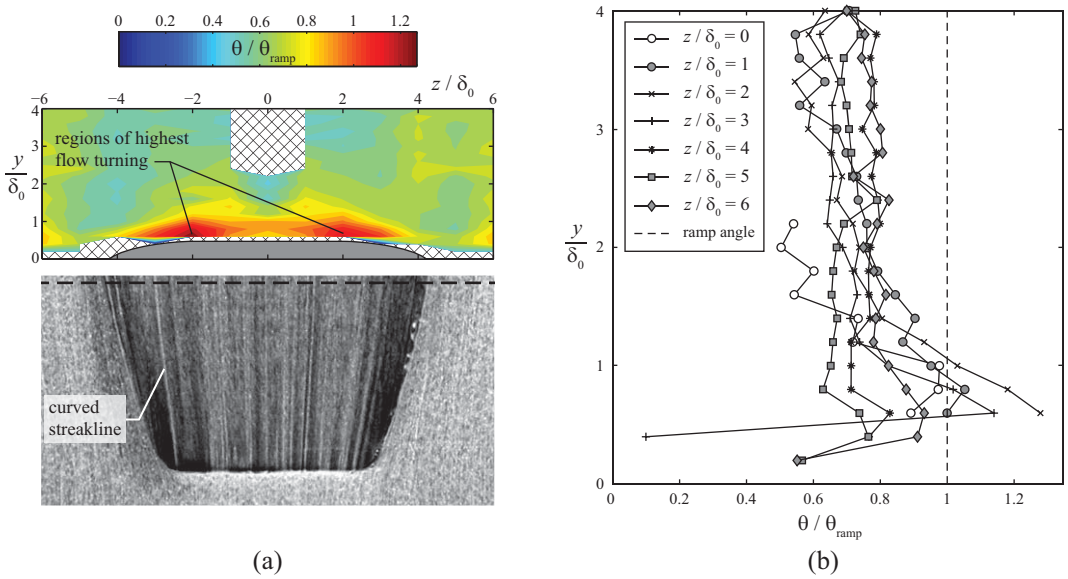

Fig. 10 Flow turning angle (relative to the floor) over the SCB ramp in a plane at $x = 5\delta_0$: (a) Contour plot (with corresponding surface oil flow image shown to scale); (b) individual plots at different span-wise positions. Angles have been calculated from two-component (u–v) velocity measurements and are plotted as a fraction of the ramp angle. Hatched areas in (a) show regions where data could not be obtained due to experimental limitations. The bump profile at this streamwise plane is shown in (a).

Close to the bump surface, figure 10b shows that the flow angle is close to the ramp angle, as expected, especially on the bump centreline ($z/\delta_0 = 0$). However, the flow angle either side of the centreline ($-3 \leq z/\delta_0 \leq -1$ and $1 \leq z/\delta_0 \leq 3$) actually exceeds the ramp angle. These local regions of high flow turning are thought to be related to flow behaviour on the bump sides (the curved part of the bump joining the ramp and the floor). Due to the increasing width of the bump in the stream-wise direction, the bump sides deflect the flow in the span-wise direction, which produces a high pressure region on the sides of the bump. This sets up a span-wise pressure gradient (which offsets the expected pressure gradient in the opposite sense) and induces a span-wise flow onto the bump ramp, compressing and decelerating the flow there and thus increasing the deflection angle. This theory is supported by the streak-lines on the bump sides which curve inwards slightly, such as the one highlighted in figure 10a. These regions of high flow turning at either edge of the bump ramp may help explain how the bump generates such a uniform degree of flow turning away from the bump in the span-wise direction.

Velocity data over the bump ramp is shown in figure 11. Regions of low momentum fluid (low streamwise velocity) are present on either side of the ramp. Vertical velocity is relatively uniform across the ramp surface and decreases with distance away from the bump.

D. SCB flow structure with a $M_\infty = 1.3$ shock upstream of the bump crest

The surface pressure distribution over the SCB, obtained from PSP measurements, is presented in figure 12. Figures 12a and 12b show overall contours of surface pressure and individual stream-wise pressure profiles respectively for the case when the shock wave is upstream of the SCB crest. The pressure profile along the surface of the bump ($z/\delta_0 = 0$) in figure 12b shows that the SCB produces the (expected) two-step pressure rise, which corresponds to the bifurcated λ-shock structure produced by the SCB when the shock is upstream of the crest. There is a noticeable pressure peak at the start of the SCB ramp ($x/\delta_0 \approx 0$) followed by a short region of gradually decreasing pressure ($2 < x/\delta_0 < 5$) due to relief effects (expansion waves originated from the bump sides) before the flow is re-compressed by the rear leg of the λ-shock structure. A small dip in pressure at $x/\delta_0 \approx 10$ suggests that the (still slightly supersonic) flow is re-expanded slightly over the bump crest before

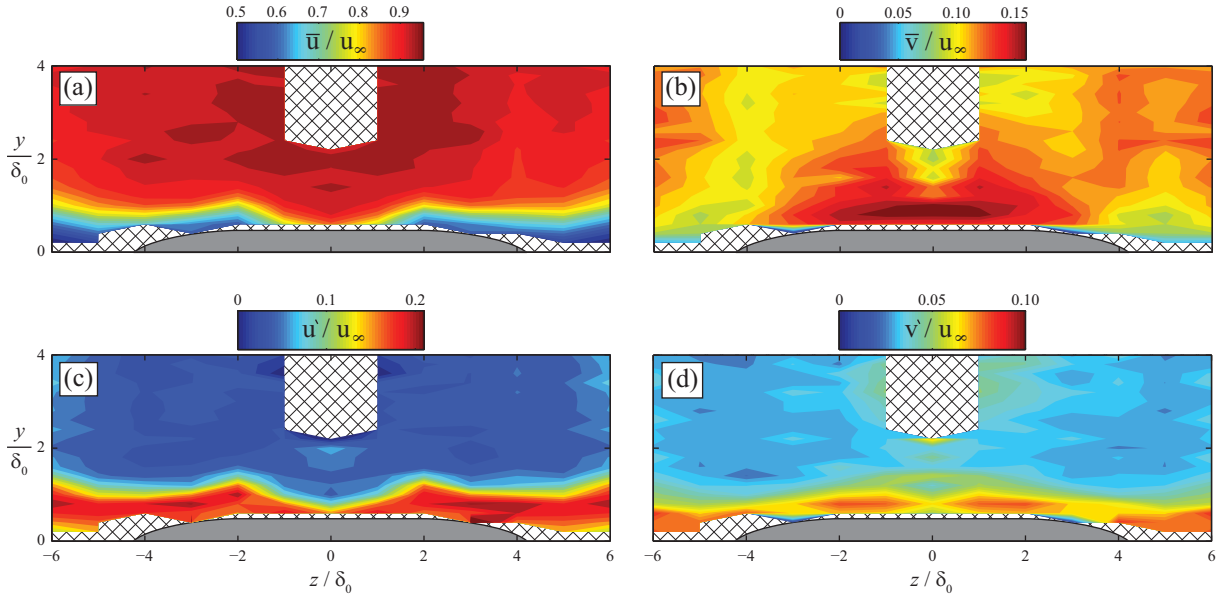

Fig. 11 Velocity contours on the SCB ramp in a plane at $x = 5\delta_0$: (a) Mean streamwise velocity; (b) mean vertical velocity; (c) fluctuating streamwise velocity; (d) fluctuating vertical velocity. Velocities have been normalised by the incoming freestream velocity u_∞. Hatched areas show regions where data could not be obtained due to experimental limitations. The bump profile at this streamwise plane is shown.

it is re-compressed by further weak "shocklets", in agreement with the schlieren image (shown to scale).

On the flat tunnel floor beside the SCB ($z/\delta_0 = -6$), the pressure rise through the shock system is more gradual and monotonic than on the SCB centreline. However, close inspection of the pressure profile at $z/\delta_0 = -6$ in figure 12b shows that the two-step pressure rise seen on the tunnel centreline does still exist, although the two parts of the pressure rise (due to the front and rear legs of the λ-shock structure) are almost completely merged and hard to distinguish between. The extent of pressure smearing due to the SCB is well-highlighted by comparison of the pressure profiles in figure 12b to those for the uncontrolled case (figure 5c). The overall pressure rise through the interaction, which appears to approach an asymptote of $p/p_{01} \approx 0.60$ at $x/\delta_0 \approx 30$ is slightly reduced in comparison with the baseline case, which has a similar shock position and reaches $p/p_{01} \approx 0.65$ (figure 5c).

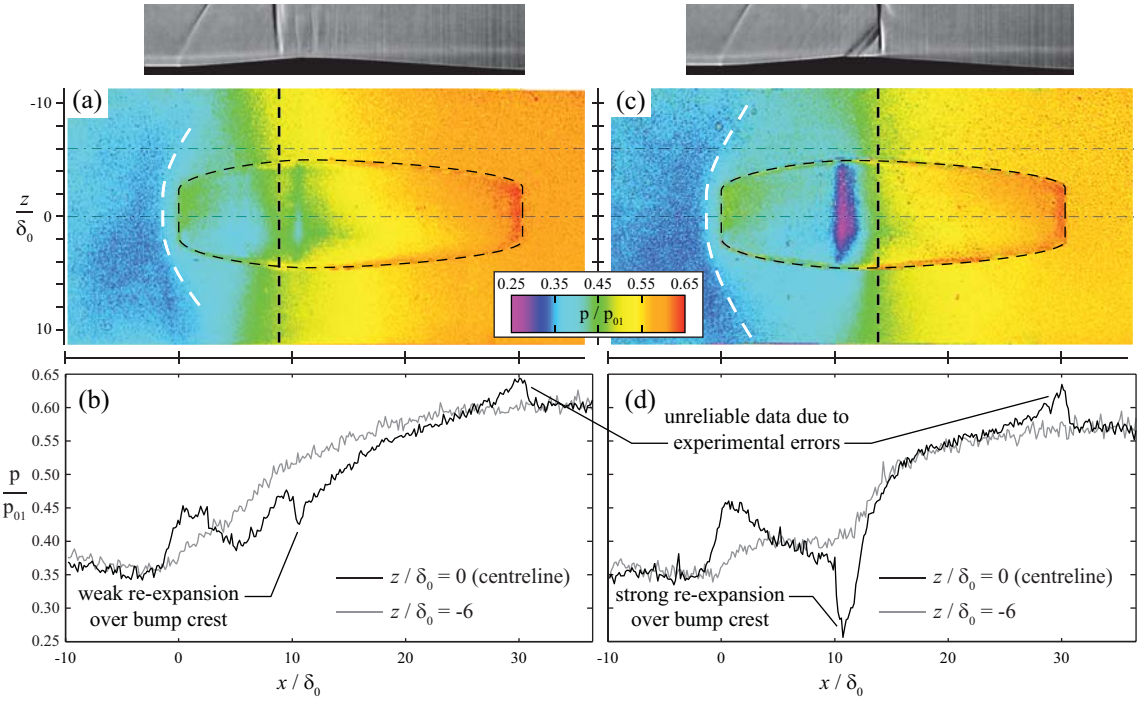

Fig. 12 Surface pressure distributions and stream-wise profiles: (a)–(b) Shock wave upstream of the SCB crest; (c)–(d) shock wave downstream of the SCB crest. PSP images show the entire width of the wind tunnel working section. The dashed black line shows the location of the shock wave. The dashed white line shows the span-wise variation of the upstream influence of the front leg of the λ-shock foot. The faint dot-dashed lines in (a) and (c) correspond to the span-wise positions of the pressure profiles in (b) and (d). The small peaks in pressure on the bump centreline at $x_s/\delta_0 = 30$ are due to experimental errors. In both cases, the pressure on the bump centreline should asymptote to the pressure at $z/\delta_0 = 6$, as is the case for $x_s/\delta_0 > 30$

Velocity contours from LDA measurements along the bump centreline with $x_s/\delta_0 = 9$ are plotted in figure 13. These velocity contours show good agreement with the schlieren image. Velocity fluctuations grow gradually along the bump, which suggests that the boundary layer remains healthy and grows slowly as the flow is compressed through the system of relatively weak shock waves. The plot of flow angle (θ) in figure 13 shows that the flow follows the surface of the SCB relatively smoothly and also supports the trend of non-uniform flow-turning in the wall-normal direction over the bump ramp, identified previously in schlieren images (figure 9) and span-wise LDA surveys of the bump ramp (figure 11).

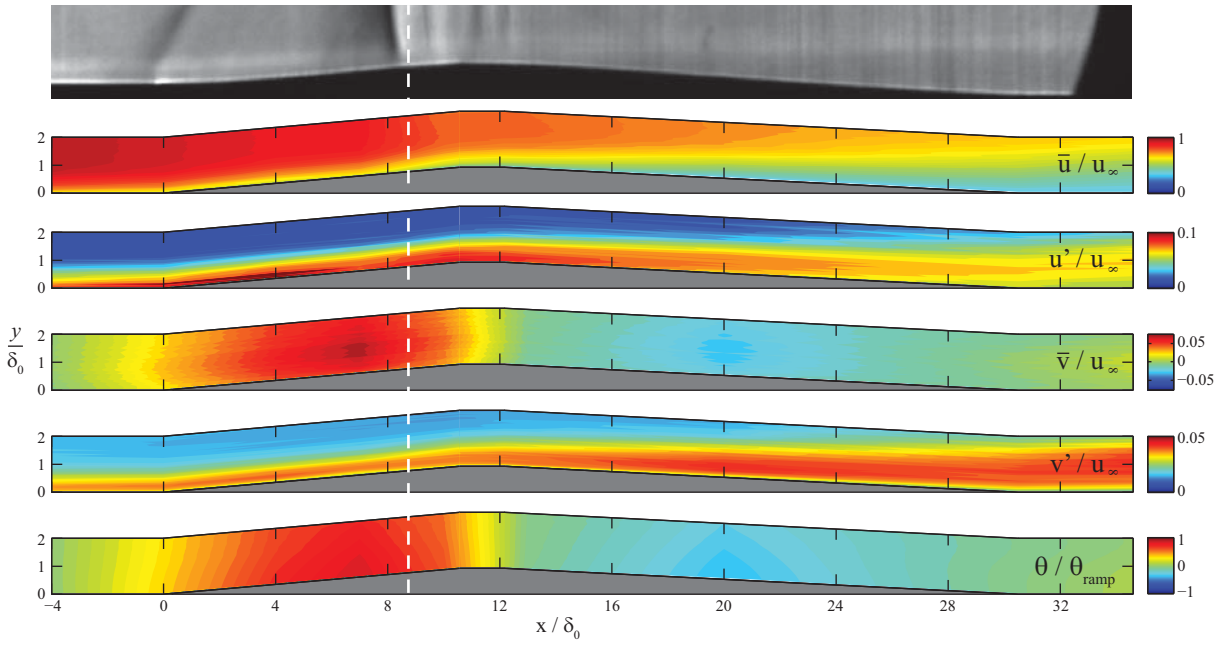

Fig. 13 Velocity contours and streamwise flow angle (θ) along SCB centreline with $x_s/\delta_0 = 9$

The bump wake with $x_s/\delta_0 = 9$ is studied in figure 14, where velocity contours from LDA measurements obtained in a span-wise plane downstream of the bump are shown. Part of the corresponding oil-flow (shown previously as figure 7c) is also shown to scale. The contour plot of mean vertical velocity in figure 14 reveals the presence of regions of up-wash and down-wash immediately downstream of the bump. These regions are consistent with the presence of a pair of counter-rotating vortices, although the relatively small vertical velocities suggests the vortices may be rather weak. These vortices are thought to originate from a three-dimensional flow separation at the bump shoulders, which can be seen as a region of oil accumulation in figure 15a. The dark areas in the oil-flow in figure 14 (which occur due to the high shear stress that is experienced directly beneath a vortex) correlate well with the expected (span-wise) vortex positions inferred from the velocity measurements. The height of the vortex centres above the floor is more difficult to determine, although they do not appear to have lifted off the surface significantly. The region of positive (upwards) vertical velocity immediately downstream of the bump is due to the up-wash effect of the vortex pair. The plots of mean and fluctuating streamwise velocity show some span-wise variation in boundary layer properties downstream of the bump, although the variations are quite

small.

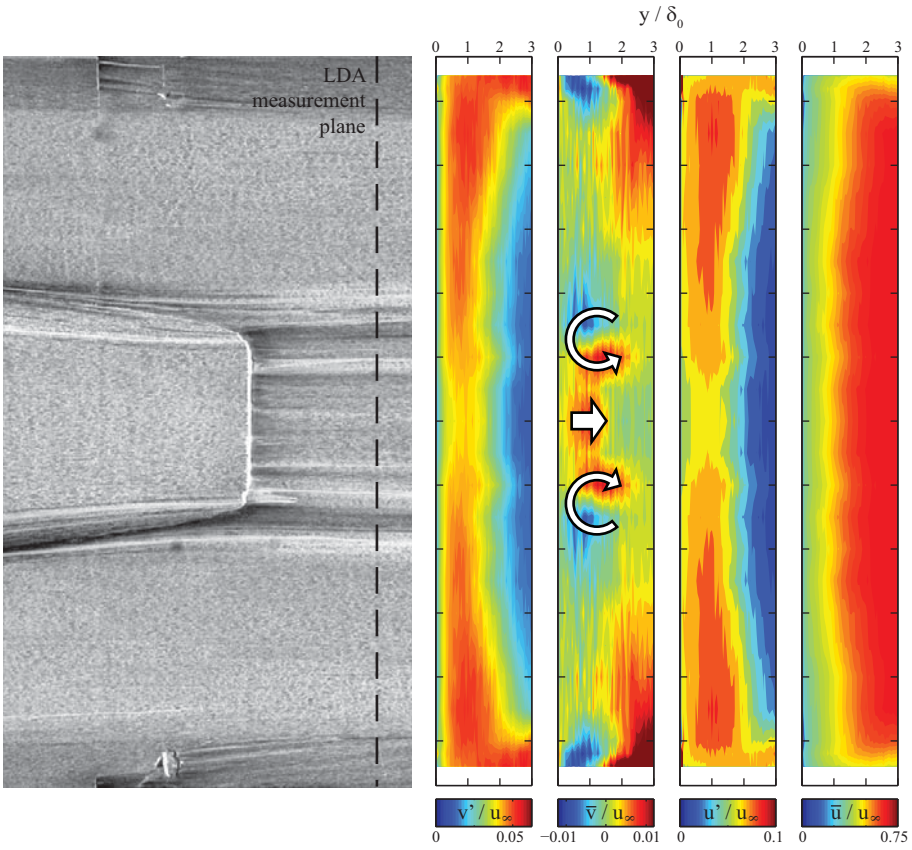

Fig. 14 Velocity contours in the SCB wake with $x_s/\delta_0 = 9$. Measurements have been obtained a distance of $4\delta_0$ downstream of the SCB trailing edge for one side only and an assumption of flow symmetry has been made

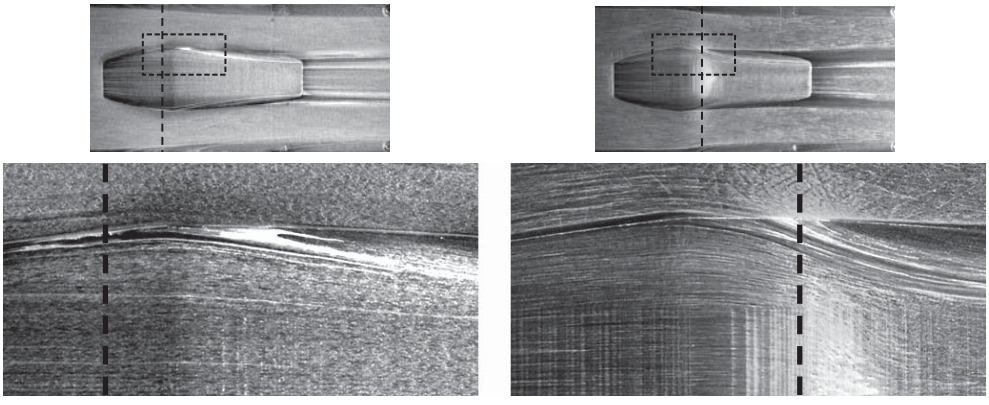

(a) (b)

Fig. 15 Close up of surface flow topology over the bump shoulder: (a) $x_s/\delta_0 = 9$; (b) $x_s/\delta_0 = 14$

E. SCB flow structure with a $M_\infty = 1.3$ shock wave downstream of the bump crest

The surface pressure distribution and individual pressure profiles over the SCB with $x_s/\delta_0 = 14$ are presented in figures 12c and 12d respectively. The pressure rise along the bump centreline initially follows a similar trend to the upstream shock position ($x_s/\delta_0 = 9$) test case, with a pressure peak at the start of the bump followed by gradual re-expansion along the bump ramp. This gradual re-expansion continues along the entire length of the bump ramp until $x/\delta_0 = 10$, where there is a sharp dip in pressure, as the (supersonic) flow is accelerated over the convex bump crest. The pressure at the crest reaches a minimum (normalised) value of 0.26, which corresponds to a peak local Mach number of around 1.53. This high local Mach number causes the rear leg of the main λ-shock structure to become very strong and leads to the small separation bubble seen in figure 8b.

To the side of the SCB (plot at $z/\delta_0 = -6$ in figure 12d), a clear two-step pressure rise can be seen. This confirms that the SCB propagates a significant shock-smearing effect in the span-wise direction, in agreement with the findings of previous studies[4]. It is likely that this extensive region of beneficial (in terms of wave drag saving) shock-smearing either side of the SCB compensates for the local region of high shock strength downstream of the SCB crest, which would produce an increased level of wave drag. The overall pressure rise through the shock structure is lower than for the upstream shock case, although this is partly due to the different shock positions relative to the downstream extent of the measurement window for PSP.

Velocity contours for the shock downstream of the bump crest are plotted in figure 16. Flow re-acceleration over the bump crest is clearly visible in the plots of mean vertical and streamwise velocities. There is a sharp rise in streamwise velocity fluctuations at $x/\delta_0 = 12$, which corresponds to the location of the leading leg of the secondary λ-shock foot structure seen in figure 6f. A similar sharp rise in vertical velocity fluctuations occurs slightly further downstream at approximately $x/\delta_0 = 13$. Comparison with the contours in figure 13 shows that the velocity fluctuations in the post-shock boundary layer are more intense when the shock is downstream of the bump crest. The other significant difference between the two cases is the region of positive vertical velocity just downstream of the bump crest at around $x/\delta_0 = 14$ in figure 16 that is not present in figure 13. This feature is further evidence of (shock-induced) flow separation.

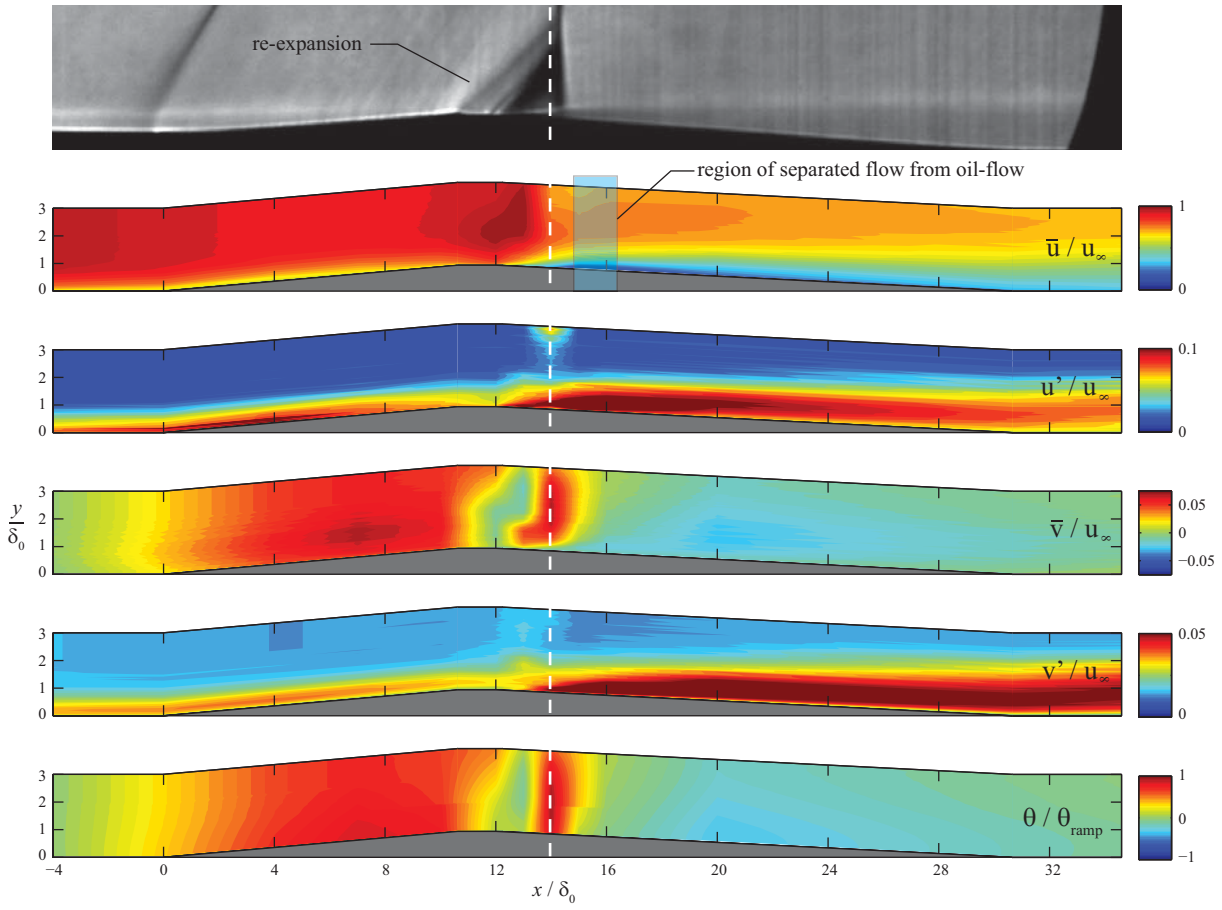

Fig. 16 Velocity contours and flow turning angle (θ) along SCB centreline with $x_s/\delta_0 = 14$

The bump wake with $x_s/\delta_0 = 14$ is analysed in figure 17. As at $x_s/\delta_0 = 9$, the plots of mean and fluctuating streamwise velocity suggest that there is relatively little span-wise variation in the post-bump boundary layer. However, the regions of high shear stress behind the bump are very dark, which suggests that either the vortices are stronger than they were at $x_s/\delta_0 = 9$ and/or that they are closer to the surface. Analysis of the vertical velocity contours in figure 17 does not yield a conclusive answer to this question, although the data does confirm the observation in the oil-flow that the vortices are spaced further apart. As with the upstream shock position, the magnitude of the vertical velocities is rather small, which suggests that the vortices are quite weak. The surface flow topology just downstream of the bump shoulder for this test case (shown in figure 15b) is noticeably different to the flow topology with $x_s/\delta_0 = 9$, suggesting that the mechanism of vortex production is strongly affected by whether the shock wave is upstream or downstream of the bump

crest. Both images in figure 15 show a region of oil accumulation just downstream of the bump crest, although the surface streamlines are more sharply deflected around this region when the shock is downstream of the crest.

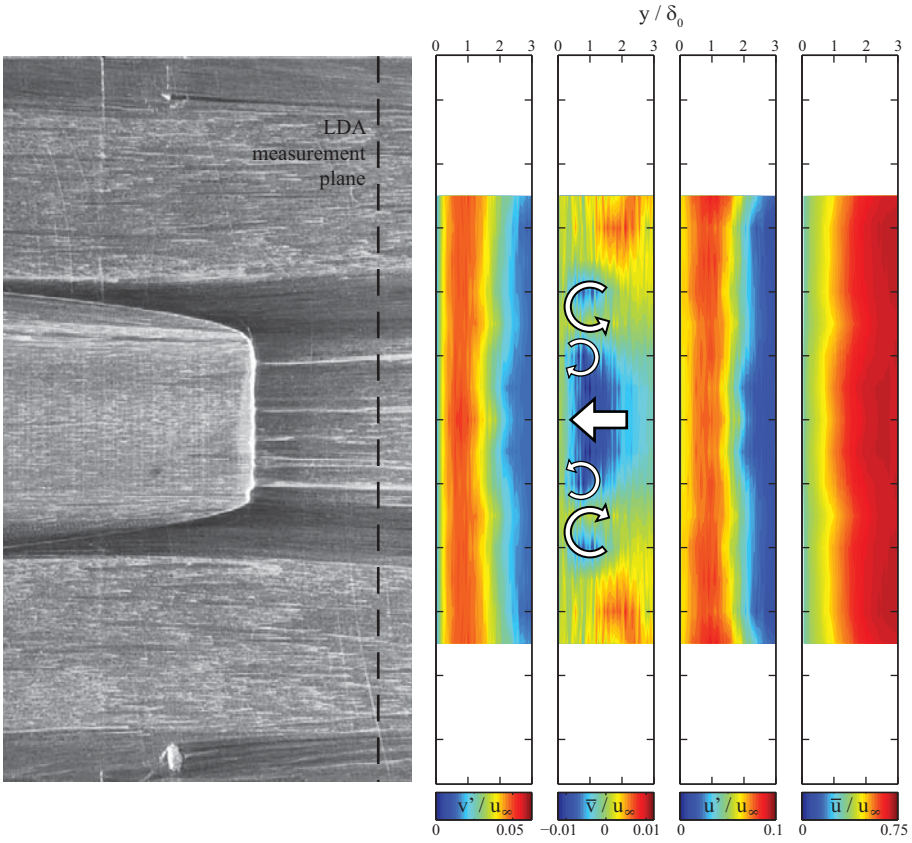

Fig. 17 Velocity contours in the SCB wake with $x_s/\delta_0 = 14$. Measurements have been obtained a distance of $4\delta_0$ downstream of the SCB trailing edge for one side only and an assumption of flow symmetry has been made

Figure 17 shows that a region of downwards velocity exists between the vortices. This is different to when the shock wave was upstream of the bump crest (see figure 14), where there was an up-wash region between the vortices. The reason for this difference is not clear, but it may be that a pair of secondary vortices exists between the main ones. It is possible that such a pair of vortices could have been formed as the flow was sharply deflected at the (three-dimensional) separation bubble just downstream of the bump crest at around $x_s/\delta_0 = 13$ or may simply have been induced by the primary vortices produced at the bump crest. The presence of a secondary vortex pair would be consistent with the increased vortex spacing relative to the $x_s/\delta_0 = 9$ case and also the region of

downwards velocity. Previous studies[4] have also suggested that 3-D SCBs may generate two pairs of counter-rotating stream-wise vortices when boundary layer separation at the bump crest occurs (see figure 3).

IV. Discussion of 3-D SCB flow physics

Prominent features of the flow over the 3-D SCB investigated here are discussed.

SCB ramp flow

The flow over the ramp of a 3-D SCB is considerably more complex than the ramp-flow on a 2-D device. Three-dimensional effects are responsible for non-uniform flow turning in both the wall-normal and span-wise directions (i.e. a $y - z$ plane over the ramp). In general, the flow angle decreases with distance away from the ramp surface, although the span-wise variation of flow turning angle is more complex. In particular, two local peaks in flow-turning that actually exceed the 2-D ramp angle exist at either side of the ramp. The observed variation in flow turning angle is due to a combination of expansion and compression waves which originate at the ramp sides. Initially (at the start of the ramp) the wall-normal deflection of the flow by the ramp dominates and the pressure on the ramp is higher than to either side and this leads to expansion waves emanating from the ramp sides to turn the flow away from the bump centreline and relieve the initial compression over the ramp. Further along the ramp however, as the height of the bump increases, span-wise turning of the flow either side of the ramp (due to the increasing bump width) becomes significant and combines with the (curved) leading leg of the λ-shock foot structure to produce regions of high pressure either side of the bump ramp, which promote span-wise flow onto the ramp at an angle that exceeds the 2-D ramp angle (due to the steep sides). These local peaks in flow angle are thought to be beneficial for the span-wise propagation of the quasi-2-D λ-shock structure generated by the bump. The presence of these competing span-wise pressure gradients is thought to limit the generation of any vorticity at the ramp sides.

SCB crest

The position of the shock wave relative to the crest determines important features of the SCB flow. The stream-wise flow onto the crest (from the bump ramp) is invariably still supersonic, which leads to re-expansion of the flow due to the convex curvature there and a local region of low pressure. This leads to a high span-wise pressure gradient at the crest, as the pressure either side of the bump is generally much higher, which encourages span-wise flow onto the SCB and the formation of vortices. When the shock is downstream of the crest, the flow is very strongly re-accelerated to high local Mach numbers, which can cause the rear leg of the main λ-shock structure to become very strong and provoke separation of the boundary layer.

SCB tail

The flow over the long SCB tail is relatively benign for all cases tested: Even when shock-induced separation occurs downstream of the crest, the flow very quickly reattaches over the start of the tail. This is attributed to the long stream-wise length of the tail, which brings the flow back to the tunnel floor very gently. The magnitude of any span-wise pressure gradient across the bump tail has a strong effect on the development of the bump wake, including the path of any vortices generated at the bump crest. When the shock is upstream of the crest, there is a significant positive pressure gradient towards the bump centreline which persists over almost the entire length of the tail and restricts the wake from spreading. In contrast, with the shock downstream of the crest, there is very little span-wise pressure gradient across the SCB tail and the wake spreads more quickly.

Vortex production and behaviour

Vortices form on the sides of the SCB at the crest location. Their formation is strongly influenced by the strength of any span-wise pressure gradient at this location and SCB geometry. When the pressure on the bump crest is very low (such as when the shock is downstream of the crest) there is a strong span-wise flow onto the SCB and relatively strong vortices are produced. As these vortices are convected downstream, their strength and trajectories are influenced by the presence of span-wise and stream-wise pressure gradients over the SCB tail. When there is a significant positive pressure gradient towards the bump centreline, the vortices follow the SCB sides on a converging trajectory

and produce a region of up-wash on the SCB centreline. When the span-wise pressure gradient over the tail is small, the vortices tend to spread out more and may (if they are strong enough) induce a pair of secondary vortices, which can produce a region of down-wash on the bump wake centreline. The stream-wise adverse pressure gradient over the SCB tail is thought to significantly weaken the vortices by the time they reach the SCB trailing edge.

V. Conclusions

Experiments investigating the flow physics of a single discrete (3-D) SCB on a flat plate with a $M_\infty = 1.3$ normal shock wave have been performed. The results from this experimental study generally support the findings of previous researchers as well as shedding new light on aspects of 3-D SCB performance. The flow over each part of the SCB (ramp, crest and tail) is analysed in detail and the effect of shock position is explored. It is found that span-wise pressure gradients across the SCB ramp affect the magnitude and uniformity of the angle of flow turning generated by the bump. This can lead to flow turning angles that exceed the 2-D ramp angle and are likely to have a (beneficial) impact on the span-wise propagation of the quasi-2-D shock structure produced by the bump. At the bump crest, a pair of counter-rotating vortices can form at the bump sides if the pressure on the crest is significantly lower than at either side of the bump. The trajectory of these primary vortices as they are convected downstream is influenced by any span-wise pressure gradients across the bump tail. If there is no significant span-wise pressure gradient and the primary vortices are sufficiently strong, then a pair of counter-rotating secondary vortices may be induced.

It should be noted that although the above comments are based on the results from tests on a single 3-D SCB geometry, many aspects of the flow features described would be applicable for 3-D SCBs with different geometries. Interestingly, the effect of shock position on 3-D SCB performance would appear to be determined not only by the size of the (beneficial) λ-shock foot region and the presence of (detrimental) secondary shock systems and flow separations, but also by the magnitude of any span-wise pressure gradients that are generated across the SCB.

References

[1] Stanewsky E., Délery J., Fulkner J., and Geissler W., *Synopsis of the project Euroshock*, Notes on Numerical Fluid Mechanics: Drag reduction by Passive Shock Control - Results of the project EUROSHOCK, 80, pp. 1–124, 2002.

[2] Stanewsky E., Délery J., Fulkner J., and de Matteis P., *Synopsis of the project Euroshock II*, Notes on Numerical Fluid Mechanics and Multidisciplinary Design: Drag reduction by shock and boundary layer control - Results of the project EUROSHOCK II, 56, pp. 1–81, 1997.

[3] Birkemeyer J., Rosemann H., and Stanewsky E., *Shock control on a swept wing*, *J. Aerospace Science and Technology*, 4, pp. 147–156, 2000.

[4] Ogawa H., Babinsky H., Pätzold M., and Lutz T., *Shock-wave / boundary-layer interaction control using three-dimensional bumps for transonic wings*, *AIAA Journal*, 46, No. 6, pp. 1442-1452, 2008.

[5] Ashill P.R., Fulkner J.L., and Shires A., *A novel technique for controlling shock strength of laminar-flow aerofoil sections*, DGLR Bericht, Part 6(92-01-022), pp. 175–183, 1992.

[6] Dargel G. and Thiede P., *Assessment of shock and boundary layer control concepts for hybrid laminar flow wing design.* Notes on numerical fluid mechanics and multidisciplinary design: Drag reduction by shock and boundary layer control - Results of the project EUROSHOCK II, 80, ch. 21, 2002.

[7] Qin N., Wong W.S., and LeMoigne, A., *Three-dimensional contour bumps for transonic wing drag reduction*, *IMechE Part G*, 222, No. 5, pp. 619–629, 2008.

[8] König B., Patzold M., Lutz T., Kramer E., Rosemann H., Richter K., and Uhlemann H., *Numerical and experimental validation of three-dimensional shock control bumps*, *AIAA J. of Aircraft*, 46, No. 2, pp. 675–682, 2009.

[9] Pätzold M., Lutz T., Kramer E., and Wagner S., *Numerical optimization of finite shock control bumps*, *AIAA Paper 2006-1054*, 2006.

[10] Wong W.S., Qin N., Sellars N., Holden H., and Babinsky H., *A combined experimental and numerical study of flow structures over three-dimensional shock control bumps*, *J. Aerospace Science and Technology*, 12, pp. 436–447, 2008.

[11] Ogawa H. and Babinsky H., *Wind-tunnel set-up for investigations of normal shock wave/boundary-layer interaction control*, *AIAA Journal*, 44, pp. 2803–2805, 2006.